

# Journal of Materials Chemistry A

Materials for energy and sustainability

Accepted Manuscript

This article can be cited before page numbers have been issued, to do this please use: L. Pineau, D. Peralta, I. Profatlova, B. Yohan, Q. Jacquet, S. Lyonnard, V. Vinci, J. Drnec and L. Simonin, *J. Mater. Chem. A*, 2026, DOI: 10.1039/D5TA09250G.



This is an Accepted Manuscript, which has been through the Royal Society of Chemistry peer review process and has been accepted for publication.

Accepted Manuscripts are published online shortly after acceptance, before technical editing, formatting and proof reading. Using this free service, authors can make their results available to the community, in citable form, before we publish the edited article. We will replace this Accepted Manuscript with the edited and formatted Advance Article as soon as it is available.

You can find more information about Accepted Manuscripts in the [Information for Authors](#).

Please note that technical editing may introduce minor changes to the text and/or graphics, which may alter content. The journal's standard [Terms & Conditions](#) and the [Ethical guidelines](#) still apply. In no event shall the Royal Society of Chemistry be held responsible for any errors or omissions in this Accepted Manuscript or any consequences arising from the use of any information it contains.

# Unveiling the irreversible structural evolution upon rehydration of Manganese-based Prussian White: an *in-situ* X-ray diffraction study

View Article Online

DOI: 10.1039/D5TA09250G

Léna PINEAU<sup>1</sup>, David PERALTA<sup>1</sup>, Irina PROFATILOVA<sup>1</sup>, Yohan BIECHER<sup>1</sup>, Quentin JACQUET<sup>2</sup>,  
Sandrine LYONNARD<sup>2</sup>, Jakub DRNEC<sup>3</sup>, Valentin VINCI<sup>3</sup>, Loïc SIMONIN<sup>1</sup>

## Affiliations

<sup>1</sup>Université Grenoble Alpes, CEA, LITEN, 17 Avenue des Martyrs, Cedex 9, Grenoble  
38054, France

E-mail: lena.pineau@cea.fr

<sup>2</sup>Univ. Grenoble, Alpes, CEA, CNRS, Grenoble INP, IRIG, SyMMES, F-38000 Grenoble,  
France

<sup>3</sup>ESRF, ID31, 71 Avenue des Martyrs, 38000 Grenoble, France

## Abstract

Manganese-based Prussian White  $\text{Na}_{2-x}\text{Mn}[\text{Fe}(\text{CN})_6]_y \cdot z\text{H}_2\text{O}$  ( $0 \leq x \leq 2$ ,  $0 \leq y \leq 1$ ) (PW) is a promising cathode material for sodium-ion batteries, due to variety of its composition, intercalation properties, and good electrochemical performance. However, water-induced structural transformations limit its practical application and remain poorly understood. To unravel how water content governs structure transformations in relation to electrochemical performance, a rehydration of a heat-treated  $\text{Na}_{1.67}\text{Mn}[\text{Fe}(\text{CN})_6]_{0.88} \cdot 0.12$  compound was monitored by *in situ* synchrotron x-ray diffraction performed under a controlled atmosphere. At a dew point of  $-8^\circ\text{C}$  and a flow rate of  $30 \text{ mL}\cdot\text{min}^{-1}$ , the original rhombohedral (dehydrated) phase transforms in 20 minutes into a newly formed disordered monoclinic structure. Water uptake induces a significant expansion of the lattice volume, and the enhanced structural disorder. Regarding the electrochemical performance, promising first discharge capacity of  $145 \text{ mAh}\cdot\text{g}^{-1}$  is obtained for the dehydrated PW, corresponding to 85% of its theoretical capacity ( $\sim 170 \text{ mAh}\cdot\text{g}^{-1}$ ). Surprisingly, the rehydrated compound demonstrates rather high capacity retention of 64%, while the hydrated compound retains only 14% of its initial capacity over 100 cycles at C/10 rate in a voltage range of 2.5 - 4 V vs  $\text{Na}^+/\text{Na}$ . This study provides new quantitative insights into the impact of exposure to humidity of PW and on its structural integrity after a heat treatment. The present work will help to implement cost-effective PW cathode materials in practice.



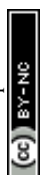
## 35 1. Introduction

View Article Online  
DOI: 10.1039/D5TA09250G

36 Li-ion batteries (LIBs) dominate the market since their first commercialisation in 1991 thanks  
37 to their good performance in terms of energy density, cycle life and energy efficiency. However,  
38 a large amount of critical raw materials is generally needed in LIB manufacturing (Li, Ni, Co,  
39 Cu etc.) which results in high commercialisation costs and could lead to geopolitical tension in  
40 the coming years.<sup>1</sup> Therefore, a promising solution is to design new battery systems composed  
41 of earth abundant elements in order to reduce the production cost below \$100/kWh by  
42 delivering the same amount of energy as current LIBs.<sup>2,3</sup> Substituting lithium, cobalt and nickel  
43 by more earth-abundant elements such as sodium, iron and manganese (e.g. sodium represents  
44 ~2.6% of the earth's crust and 3.3% in seawater) will allow to considerably  
45 decrease a battery cost.<sup>2</sup> Moreover, replacing the copper current collector (a critical raw  
46 material in LIBs) with aluminium is feasible in SIBs, as sodium does not form an alloy with  
47 aluminium. From this point of view, since the late 2000s, there is a renewed interest for the  
48 Sodium-Ion Battery technology (SIBs).<sup>4</sup> Nevertheless, the resulting energy density of SIBs is  
49 still lower compared to lithium battery technology and, therefore, higher energy density  
50 cathodes are required.

51 Prussian blue analogues (PBAs) are promising cathode materials for SIBs. Their theoretical  
52 gravimetric energy density are competitive with some Li-ion cathode materials such as LiFePO<sub>4</sub>  
53 (LFP) (e.g. 578 Wh.kg<sup>-1</sup> for Na<sub>2</sub>MnFe(CN)<sub>6</sub> as compared with 595 Wh.kg<sup>-1</sup> for LFP).<sup>5,6</sup> PBAs  
54 have the following general chemical formula A<sub>x</sub>Ma[Mb(CN)<sub>6</sub>]<sub>y</sub>□<sub>1-y</sub>zH<sub>2</sub>O. A is an alkaline  
55 earth or alkali metal (generally Na, K or Li), Ma and Mb are Transition Metal (TM) cations  
56 (often Fe or Mn) linked together by CN groups.<sup>2</sup> These materials consists of a three-dimensional  
57 network composed of MaN<sub>6</sub> and MbC<sub>6</sub> octahedra.<sup>2</sup> The PBA compounds are classified in three  
58 categories, depending on the amount of Na introduced in the lattice, and hence the oxidation  
59 state of the transition metals. The Berlin Green (BG) material is completely oxidized and thus  
60 desodiated, the Prussian Blue (PB) is partially reduced and thus sodiated and the Prussian White  
61 (PW) is completely reduced and thus exhibits two sodium atoms in its theoretical formula  
62 (Na<sub>2</sub>Ma[Mb(CN)<sub>6</sub>]<sub>y</sub>□<sub>1-y</sub>zH<sub>2</sub>O).<sup>7-9</sup> PB compound originally contains only Fe atoms in its  
63 structure, and is generally referred to as Fe-Fe composition. However, a substitution of Fe in  
64 the Ma sites by other TMs such as Mn or Cu can occur, leading to Mn-Fe or Cu-Fe compounds,  
65 respectively.<sup>10-13</sup>

66 PWs are very promising cathode materials due to the diversity of composition depending on  
67 synthesis conditions, and their high specific capacity (theoretical capacity of ~170 mAh.g<sup>-1</sup> at



68 3.5 V vs Na<sup>+</sup>/Na).<sup>6</sup> Moreover, the material production is based on simple and safe synthesis  
69 protocols (aqueous synthesis without excessive energy-consuming processes or use of toxic  
70 solvent) relying on abundant elements that crystallise in a structure favourable for Na<sup>+</sup>  
71 intercalation.

72 However, numerous technical barriers impede wide commercialization of SIBs with PW-based  
73 cathodes. One of the main challenges is deep understanding of changes in the crystallographic  
74 structure depending on several critical parameters. For example, the amount of water has a great  
75 influence on the structure of the material and, thus, the electrochemical properties. It is known  
76 that a significant amount of water in the forms of surface water, interstitial water, or coordinated  
77 water can present in the structure, and may exceed 20% of its total mass after synthesis.<sup>2,14,15</sup>  
78 Coordinated water molecules are linked to the transition metal cyanide network, and fill  
79 M<sub>b</sub>(CN)<sub>6</sub> vacancy defects, generally represented by a lack of ferrocyanide anion [Fe(CN)<sub>6</sub>]<sup>4-</sup>  
80 in the lattice.<sup>2,3,10,14,16</sup> From this point of view, the coordinated water content highly depends on  
81 the synthesis conditions as these greatly influence the formation of Fe(CN)<sub>6</sub> vacancies.<sup>2</sup> This  
82 coordinated water cannot be removed by heat treatment as temperatures exceeding the PBA's  
83 decomposition temperature (higher than 200°C) would be needed, unlike interstitial or adsorbed  
84 water which are more weakly bound and thus easier to remove.<sup>14,17,18</sup> Interstitial water occupies  
85 the Na<sup>+</sup> vacancies, while the adsorbed water only interacts physically with the crystal surface.  
86 The interstitial and adsorbed water amounts are also determined by the synthesis  
87 conditions<sup>12,14,16</sup>. Hence, the presence of interstitial water also affects the crystallographic  
88 structure. Besides inducing structural changes, the water molecules can slow down the reaction  
89 kinetics during cycling by hindering Na<sup>+</sup> migration. Additionally, water can cause a lower  
90 coulombic efficiency due to side reactions during charging up to 3.8V.<sup>11,19,20</sup> It is therefore  
91 important to understand simultaneously how water content modifies the crystal structure and  
92 impacts the electrochemical performance.

93  
94 The role of interstitial water and its influence on electrochemical performance has been deeply  
95 studied for Fe-Fe compounds.<sup>3,4,21-23</sup> PBAs containing manganese (Mn) as transition metals  
96 (Mn-Fe compounds) have been extensively studied because they reveal a higher average  
97 operating potential (3.5 V) than Fe-Fe compounds (3.2 V).<sup>3,4,10,24</sup> The fully sodiated PW  
98 compound (Na<sub>2</sub>Mn<sup>II</sup>[Fe<sup>II</sup>(CN)<sub>6</sub>]<sub>□<sub>1-y</sub></sub>·zH<sub>2</sub>O) exhibits a monoclinic structure in the presence of  
99 interstitial water. Song *et al.* studied the role of interstitial water on crystal structure and  
100 electrochemical performance in a Na<sub>2-δ</sub>MnFe(CN)<sub>6</sub>·zH<sub>2</sub>O compound. They reported a P2<sub>1/n</sub>  
101 space group for an air-dried PW while observing a R $\bar{3}$  space group for a vacuum-dried PW.



102 Both samples were dried at 100°C.<sup>10</sup> Similarly, most studies agree that hydrated PW adopts a  
103 monoclinic  $P2_1/n$  structure, whereas the dried form exhibits a rhombohedral  $R\bar{3}$   
104 structure.<sup>11,19,24,25</sup> Furthermore, several studies have already reported the influence of  
105 rehydration on dehydrated PW structure. Under air exposure, the rhombohedral structure  
106 evolves back to a monoclinic one by capturing H<sub>2</sub>O molecules inside the lattice (interstitial  
107 water).<sup>15,18,24,26,27</sup> For example, Hartmann *et al.* studied chemical and structural changes under  
108 humidity exposure of a PBA compound Na<sub>1.8</sub>Mn<sub>0.8</sub>Fe<sub>0.2</sub>[Fe(CN)<sub>6</sub>]<sub>0.9</sub>·zH<sub>2</sub>O. This material  
109 exhibits a rhombohedral structure after a drying process at 150 °C and converts back to the  
110 monoclinic structure upon humid air exposure with slightly broader peaks than the cubic phase  
111 from a pristine sample Na<sub>1.3</sub>Mn<sub>0.8</sub>Fe<sub>0.2</sub>[Fe(CN)<sub>6</sub>]<sub>0.9</sub>·zH<sub>2</sub>O. More recent reports considered the  
112 structural behaviour of dried samples under ambient air. Wang *et al.* studied structural  
113 characteristics of a Na<sub>2-x</sub>Mn<sub>0.8</sub>Fe<sub>0.2</sub>[Fe(CN)<sub>6</sub>]<sub>y</sub>·nH<sub>2</sub>O (0 ≤ x ≤ 2, 0 ≤ y ≤ 1) compound during the  
114 dehydration and rehydration processes and quantified the correlation among water content,  
115 structure, defects, and electrochemical properties. Using ICP and elemental analyses, they  
116 showed that [Fe(CN)<sub>6</sub>] defects significantly increase during a dehydration process ,  
117 accompanied by structural damage.<sup>18</sup> Moreover, Clavelin *et al.* examined the dehydration and  
118 rehydration processes of a PW Na<sub>1.87</sub>Mn[Fe(CN)<sub>6</sub>]<sub>0.99</sub>·1.99 H<sub>2</sub>O sample synthesized by an  
119 aqueous co-precipitation method. They studied the rehydration of a dehydrated sample vacuum-  
120 dried at 150 °C for 20 h (20 mbar). They found a rhombohedral structure evolving under air  
121 exposure into monoclinic phase in about 30 min for compact powder and less than 5 min for an  
122 electrode.<sup>24</sup> In a recent report, Li *et al* synthesized a Na<sub>1.95</sub>Mn[Fe(CN)<sub>6</sub>]<sub>0.91</sub>·□<sub>0.09</sub>·0.08 H<sub>2</sub>O  
123 compound and demonstrated a fast re-absorption of water under ambient conditions, converting  
124 a rhombohedral phase back to a monoclinic phase. Considering the fast kinetics of the process,  
125 accurate monitoring under laboratory conditions is challenging, as it requires fast scanning  
126 techniques to capture transient features with sufficient angular resolution. Therefore, despite  
127 the large volume of re- and de-hydration research carried out on PWs, a deeper understanding  
128 of the structural evolution under controlled water uptake of dehydrated MnFe through the  
129 analysis of the phase content evolution is required. This work aims to be able to track in real  
130 time and precisely the details of the insertion of water molecules in the lattice and evaluate how  
131 their content and type affect electrochemical performance.

132 Herein, we report a PW Na<sub>1.67</sub>Mn[Fe(CN)<sub>6</sub>]<sub>0.88</sub>, □<sub>0.12</sub>, 2,5 H<sub>2</sub>O synthesized using a precipitation  
133 method from Na<sub>4</sub>Fe(CN)<sub>6</sub>, 10H<sub>2</sub>O and Mn(NO<sub>3</sub>)<sub>2</sub>, 4H<sub>2</sub>O precursors. After drying at 180°C  
134 under high vacuum (10<sup>-2</sup> mbar), the material adopts a rhombohedral  $R\bar{3}$  phase, as shown by  
135 XRD. The material structure evolution is followed under an exposure to the atmosphere with



136 controlled humidity by time-resolved synchrotron *operando* X-ray Diffraction (SXRD)  
 137 Infrared spectroscopy, Thermogravimetric Analyses and Mossbauer analyses are used to assess  
 138 the influence of water content on physico-chemical properties of the material. A reversible cycle  
 139 of water desinsertion-insertion was observed at a local scale, however an irreversible  
 140 phenomenon occurs at a particle scale regarding the difference in lattice parameters.  
 141 Galvanostatic cycling is compared for hydrated, dehydrated and rehydrated  
 142  $\text{Na}_{1.67}\text{Mn}[\text{Fe}(\text{CN})_6]_{0.88, \square_{0.12}}$ , 2,5  $\text{H}_2\text{O}$  samples after ambient air exposure. Promising first  
 143 discharge capacity of  $145 \text{ mAh.g}^{-1}$  for the dehydrated PW is obtained. Surprising capacity  
 144 retention of 64% is obtained for the rehydrated compound over 100 cycles at C/10 rate vs  
 145  $\text{Na}^+/\text{Na}$ , while the hydrated compound retains only 14% of its initial capacity.

## 147 2. Methods section

### 148 2.1. Material synthesis

149 All the samples were synthesized by using commercial reactants: sodium ferrocyanide  
 150 decahydrate (Sigma Aldrich®,  $\text{Na}_4\text{Fe}(\text{CN})_6 \cdot 10\text{H}_2\text{O}$ , 99%), manganese nitrate tetrahydrate  
 151 (Sigma Aldrich®,  $\text{Mn}(\text{NO}_3)_2 \cdot 4\text{H}_2\text{O}$ , 97%), and sodium citrate tribasic dihydrate (Sigma  
 152 Aldrich®,  $\text{C}_6\text{H}_5\text{Na}_3\text{O}_7 \cdot 2\text{H}_2\text{O}$ , 99%). All reactants were used without further purification. The  
 153 synthesis of PW,  $\text{Na}_{2-x}\text{Mn}[\text{Fe}(\text{CN})_6]_y \cdot \square_{1-y} \cdot z\text{H}_2\text{O}$ , was carried out by a simple precipitation  
 154 method (Figure S1). Specifically, a solution of 250 mL of  $\text{Na}_4\text{Fe}(\text{CN})_6 \cdot 10\text{H}_2\text{O}$  (15 g) was  
 155 prepared and introduced in a reactor. A second solution of 750 mL of  $\text{Mn}(\text{NO}_3)_2 \cdot 4\text{H}_2\text{O}$  (8 g)  
 156 and sodium citrate (65 g) was prepared in a bottle. The second precursor's solution was  
 157 introduced in the reactor under stirring at 1000 rotations per minutes (rpm). The synthesis was  
 158 achieved when the second solution was completely introduced into the reactor. The obtained  
 159 solution was left to age during 16 hours at room temperature. The obtained precipitate was  
 160 washed three times with deoxygenated water and placed under vacuum at room temperature  
 161 overnight. After being grounded in a mortar, the as-prepared compound is designated MnPW-  
 162 H, where H refers to Hydrated. Then, MnPW-H powder was dried under strong vacuum ( $10^{-2}$   
 163 mbar) at  $180 \text{ }^\circ\text{C}$  during 16 hours with a ramping rate of  $6^\circ\text{C.min}^{-1}$  to become a dehydrated  
 164 powder MnPW-D (D refers to Dehydrated). MnPW-R (R refers to Rehydrated) was designated  
 165 as MnPW-D exposed under ambient air. All samples' descriptions are summarized in Table 1.

166 Table 1: Sample nomenclature

Sample name	Description	Comments
-------------	-------------	----------



MnPW-H	Hydrated	As-synthesized compound
MnPW-D	Dehydrated	As-synthesized compound dried at 180°C under vacuum
MnPW-R	Rehydrated	Dried compound exposed at ambient air during 24 h

View Article Online  
DOI: 10.1039/D5TA09250G

167

## 168 2.2. Synchrotron X-Ray Diffraction under humidity-controlled atmosphere

169 Synchrotron *in-situ* X-ray Diffraction (SXR) patterns were collected at the ID31 beamline of  
170 the European Synchrotron Radiation Facility (ESRF) in Grenoble, with an energy of 75 keV.  
171 The X-ray beam size was 200  $\mu\text{m}$  vertically and 400  $\mu\text{m}$  horizontally. The measurements were  
172 conducted between 1.2° and 24.6° by packing about 5 mg of powder into 4 mm outer diameter  
173 (O.D.) and 2.04 mm inner diameter (I.D.) quartz glass capillaries. The capillary was loaded  
174 with the powder and tightly closed in an Ar-filled glove box (O<sub>2</sub> and H<sub>2</sub>O concentrations less  
175 than 0.1 ppm). Then, the sample was transferred to the beamline and connected to the gas line.  
176 The *in-situ* rehydration was performed using a home-made test assembly built around the  
177 beamline. Argon carrier gas was supplied at a flow of 30 mL.min<sup>-1</sup> and humidified at a dewpoint  
178 of -8 °C using Cellkraft® humidifier. After being humidified, Ar flow was forced through the  
179 airtight capillary containing the dehydrated powder MnPW-D. SXR patterns were acquired  
180 every 7 s. The air tightness of the capillary was ensured using Swagelok® connections with  
181 Teflon® gaskets in contact with the glass cell to prevent its damaging. A system of automatic  
182 valves was used to control the gas flow remotely. The data can be found at  
183 <https://doi.org/10.15151/ESRF-DC-2248221589>.

184 Furthermore, *ex situ* measurements were conducted at the beamline on pristine powder  
185 (MnPW-H) and rehydrated powder after one day under air-exposure (MnPW-R). The  
186 measurements were conducted between 0.1° and 17.1° with an energy of 75 keV. Identical  
187 capillaries were used and loaded with approximately 5 mg of powder at ambient air.

188 All selected diffractograms were refined by Rietveld method using Fullprof WinPLOTR.

189

## 190 2.3. Laboratory X-Ray Diffraction

191 X-ray diffraction (XRD) experiments were performed on a Bruker Advance X-ray  
192 diffractometer, equipped with a Cu target X-Ray (1.54056 Å) between 8 ° and 70 °. These  
193 measurements were only conducted on rehydrated powders (MnPW-R, MnPW-R2 and MnPW-  
194 R3).



195

## 196 2.4. Elemental analysis

197 Elemental analysis was performed by ICP-OES measurements were performed on the PW  
198 powders after synthesis. The samples were dissolved by microwave digestion with a mix of  
199 HNO<sub>3</sub>, HCl and HF acid. The mineralization was complete.

200 The water content of the electrodes was quantified using a Karl Fischer Moisture Titrator  
201 (Metrohm).

202

## 203 2.5. Fourier Transform infrared (FTIR) spectroscopy

204 FTIR experiments were performed to confirm the structure of the samples and the presence of  
205 water, on a FTIR from Thermo Scientific Nicolet iS50. The measurements were carried out  
206 with diamond crystal Attenuated Total Reflectance (ATR) accessory. The samples were  
207 analysed under air and under argon in a sealed cell for the hydrated samples (MnPW-H and  
208 MnPW-R) and the dried sample (MnPW-D), respectively. Both samples were analysed between  
209 400 cm<sup>-1</sup> and 4000 cm<sup>-1</sup>.

210

## 211 2.6. Thermal analysis

212 The thermal evolution and the water content of the material were observed with  
213 Thermogravimetric analysis (TGA). The data was collected on a TGA550 model from SAS  
214 WATERS company under argon with a constant heat ramp rate of 10 °C/min until a final  
215 temperature of 550 °C. The samples were measured in sealed aluminium crucibles.

216

## 217 2.7. Morphology and particle size distribution

218 The particles morphology was observed by Scanning Electron Microscopy (SEM, Zeiss Sigma  
219 300), with an operating voltage of 5 kV. The particle size distribution was performed on a laser  
220 diffraction particle size analyser from Anton Paar company. The measurements were realised  
221 in water solvent after 10 minutes under ultrasound.

222

## 223 2.8. Mössbauer spectroscopy



224 Mössbauer spectroscopy were performed on hydrated samples (MnPW-H and MnPW-R) and  
225 dried samples (MnPW-D). Mössbauer spectra were recorded at room-temperature on a  
226 homemade spectrometer operating in a constant acceleration mode in transmission geometry.  
227 The analysis velocity was ranging between  $-6$  and  $+6$   $\text{mm}\cdot\text{s}^{-1}$ . They were analysed with  
228 WMOSS software (WMOSS4 Mössbauer Spectral Analysis Software, [www.wmoss.org](http://www.wmoss.org), 2009-  
229 2016). The isomer shifts are referenced against that of a metallic iron foil at room-temperature.

## 231 2.9. Electrochemical tests

232 All electrodes were manufactured using an organic-based formulation. The positive electrode  
233 slurry was prepared by mixing 70 wt% of active material PW  $\text{Na}_{2-x}\text{MnFeCN}_6$ , 20 wt% of Super  
234 C65 carbon black and 10 wt% of polyvinylidene fluoride (PVDF) as binder. N-methyl-2-  
235 pyrrolidone (NMP) was used to adjust the viscosity of the slurry. The latter was coated on an  
236 aluminium foil with a thickness of 100  $\mu\text{m}$ , and dried at 55°C overnight for the hydrated and  
237 rehydrated powder. Before entering the glovebox in order to prepare the coin cells, the  
238 electrodes from the hydrated and rehydrated powder were dried at 80 °C. The electrode  
239 preparation process for the dried powder was carried out in a glovebox, and the slurry was dried  
240 in a vacuum oven. All electrodes were punched out with a diameter of 14 mm and calendared  
241 at a pressure of 1 ton. The mass loading of the electrode active material was about 1  $\text{mg}\cdot\text{cm}^{-2}$ .

242 The electrochemical half-cells were assembled in an argon-filled glovebox. Half cells were  
243 assembled with a PW positive electrode, one separator of glass fibre filter paper (Whatman  
244 GF/D), and a negative electrode of Na metal for all coin cells. The electrolyte was composed  
245 by 1 mol.  $\text{L}^{-1}$  of  $\text{NaPF}_6$  dissolved in ethylene carbonate (EC) and dimethyl carbonate (DMC)  
246 with a volume ratio of 50:50 mixed with 2 wt% of fluoroethylene carbonate (FEC). The  
247 electrochemical test for the charge-discharge cycles was carried out in 2032-type coin cells,  
248 using Arbin battery testing system. The galvanostatic tests were performed in a voltage range  
249 of 2.5 - 4 V (vs  $\text{Na}^+/\text{Na}$ ), with a C-rate of C/10. The specific capacities and the current rate are  
250 calculated based on a theoretical capacity of 171  $\text{mAh}\cdot\text{g}^{-1}$  for  $\text{Na}_2\text{Mn}[\text{Fe}(\text{CN})_6]$ . All  
251 electrochemical tests were performed at 25°C. The Galvanostatic Intermittent Titration  
252 Technique (GITT) and Electrochemical Impedance Spectroscopy (EIS) were performed on a  
253 Biologic battery testing system. The GITT was applied using a C-rate of C/10 in the voltage  
254 range from 2.5 to 4.0 V (vs.  $\text{Na}^+/\text{Na}$ ), with 5 cycles performed at each C-rate. The half-cell was  
255 alternately charged for 10 min at current density of 20  $\text{mA}\cdot\text{g}^{-1}$  followed by 120 min resting,



256 then discharged in the same way. The procedure was repeated for the full voltage range of  
 257 operation. The Na<sup>+</sup> diffusion coefficient ( $D_{Na^+}$ ) was calculated by using the following simplified  
 258 Eq. (1), based on Fick's second law<sup>19</sup> :

$$D_{Na^+} = \frac{4}{\pi\tau} \left(\frac{nV}{S}\right)^2 \left(\frac{\Delta E_s}{\Delta E_\tau}\right)^2 \quad (1)$$

259  
 260 Where  $n$  and  $V$  represent the molar mass (mol) and the molar volume (cm<sup>3</sup>.mol<sup>-1</sup>) of the MnPW  
 261 material, respectively.  $\tau$  signifies the time duration of a current pulse, and  $S$  is the geometrical  
 262 surface of the positive electrode.  $\Delta E_\tau$  represents the voltage variation caused by  
 263 charging/discharging in a single-step GITT process, and  $\Delta E_s$  is the equilibrium voltage variation  
 264 during a current pulse in two adjacent GITT process.

265 The EIS was examined before cycling, after one cycle, and after 5 cycles. The frequency range  
 266 was set from 1000 MHz to 10000 mHz, with an applied amplitude of 20 mV.

267

## 268 3. Results and discussions

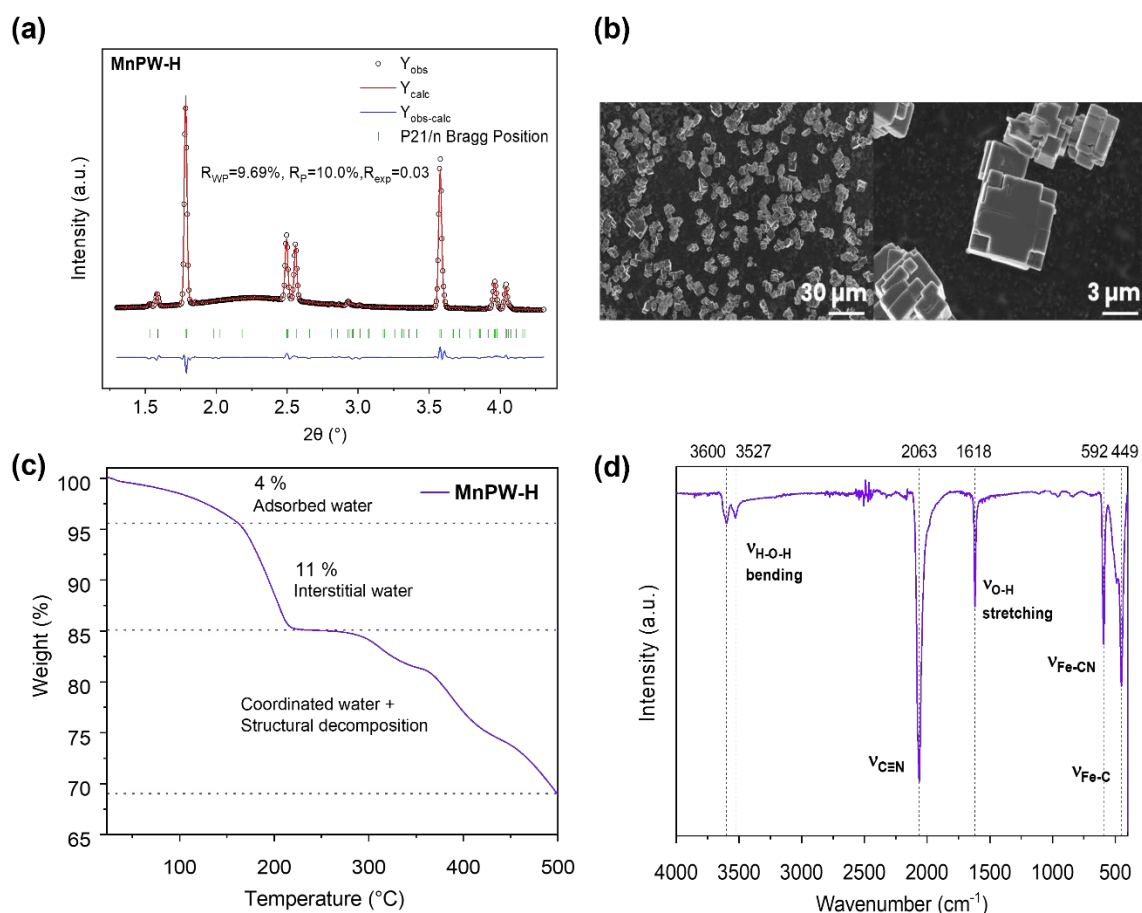
### 269 3.1. Structure of the hydrated compound

270 MnPW-H was prepared by a precipitation synthesis method and characterized in this initial  
 271 section. SXRD analysis was firstly carried out. The pattern is shown in Figure 1 (a) and vertical  
 272 lines indicate characteristic peaks for the monoclinic P2<sub>1</sub>/n phase, space group P2<sub>1</sub>/n,  
 273 confirming a well-crystallized structure and a pure phase, as already observed in the  
 274 literature.<sup>10,11,24</sup> The lattice parameters and the atomic positions were refined by the Rietveld  
 275 method. The values of the lattice parameters are as follows:  $a = 10.582(1)$ ,  $b = 7.555(1)$ ,  $c =$   
 276  $7.382(2)$  Å, and  $\beta = 92.03(3)^\circ$ . The atomic positions are shown in Table S1 in Supporting  
 277 Information. SEM on MnPW-H was carried out and the obtained images are shown in Figure 1  
 278 (b). Cubic-shaped primary particles are observed, with a typical size of around 4 μm. This  
 279 average size was confirmed by laser diffraction technique (Figure S2 and Table S2). In order to  
 280 confirm the presence and quantify the amount of water in the hydrated sample, TGA and ATR-  
 281 FTIR analyses were performed on MnPW-H (Figure 1 (c) and (d)). The TGA analysis exhibits  
 282 three distinct weigh losses from 0 °C to 160 °C, from 160 °C to 210 °C and from 320 °C to 380  
 283 °C. According to several publications, the first loss, up to 160°C, can be assigned to adsorbed  
 284 water, while the second step corresponds to interstitial water. The last step can be attributed to  
 285 the decomposition of the structure.<sup>10,24</sup> It can be seen a weight loss of 4 % of adsorbed water  
 286 and 11 % of interstitial water. Assuming that the material is dehydrated after removing adsorbed



287 and interstitial water, it can be deduced that at least 2.5 molecules per unit formula of  $\text{H}_2\text{O}$  are  
 288 present in the material, considering that the dehydrated molar mass ( $280 \text{ g}\cdot\text{mol}^{-1}$ ) is  
 289 corresponding to 86% of the total mass. Then, ATR-FTIR spectra shows two peaks at  $3600 \text{ cm}^{-1}$   
 290  $^1$  and  $3527 \text{ cm}^{-1}$  and one sharp peak at  $1617 \text{ cm}^{-1}$ , corresponding to H-O-H bending and O-H  
 291 stretching, respectively. The first H-O-H bending at  $3600 \text{ cm}^{-1}$  is characteristic of adsorbed  
 292 water, while the other two peaks confirm the presence of interstitial water in the structure, as  
 293 described by Song *et al.*<sup>10</sup> Sharp peaks at  $592 \text{ cm}^{-1}$  and  $449 \text{ cm}^{-1}$  are indexed to be Fe-CN and  
 294 Fe-C bonds, respectively. The most intense peak at  $2063 \text{ cm}^{-1}$  is attributed to the  $\text{C}\equiv\text{N}$  triple  
 295 bond.<sup>10,28</sup> The sample elemental composition was determined by ICP-OES analysis (Table S3).  
 296 From this analysis, we could determine the experimental anhydrous formula to be  
 297  $\text{Na}_{1.67}\text{Mn}[\text{Fe}(\text{CN})_6]_{0.88}, \square_{0.12}$ . Finally, according to the TGA and ATR-FTIR analyses, the final  
 298 formula of the sample would be  $\text{Na}_{1.67}\text{Mn}[\text{Fe}(\text{CN})_6]_{0.88}, \square_{0.12} 2.5 \text{ H}_2\text{O}$ .

299 As mentioned above, the dehydrated sample transforms its rhombohedral structure  $R\bar{3}$  into a  
 300 monoclinic under air exposure.<sup>15,24,26</sup> Hence, MnPW-H was dried under vacuum ( $10^{-2}$  mbar) at  
 301  $180 \text{ }^\circ\text{C}$  to become MnPW-D.



302



303 **Figure 1.** Properties of the pristine material: SXRD pattern (a), SEM observations (b), TGA analysis at 10 °C.min<sup>-1</sup> under argon atmosphere until 500°C (c) and ATR-FTIR measurements (d) of the hydrated powder  
304 MnPW-H  
305

View Article Online  
DOI: 10.1039/D5TA09250G

### 306 3.2. In situ rehydration study by SXRD

307 The structural parameters evolution of MnPW-D sample exposed to humidity is described in  
308 this following analysis. In order to follow the evolution of the material's structure during its  
309 rehydration under humidity-controlled atmosphere (dew point of -8°C) with high resolution,  
310 synchrotron patterns were collected at the ID31 beamline of the ESRF in Grenoble, with an  
311 energy of 75 keV. Quartz glass capillary filled with the powder sample was purged with humid  
312 argon. *In-situ* SXRD profiles of the water uptake of the dehydrated material MnPW-D are  
313 shown in Figure 2 (a). The 011 reflection peak from monoclinic P2<sub>1</sub>/n phase and the 012  
314 reflection peak from rhombohedral R $\bar{3}$  phase appear respectively at 1.25° and 1.3°. We can  
315 observe that MnPW-D transforms into the monoclinic phase (P2<sub>1</sub>/n) in the first minutes of the  
316 experiment. Rietveld refinements were realized on the 30 different scans presented in Figure  
317 S3 to Figure S5, from 0 to 60 minutes. The correlation table between the scan number and the  
318 time in minute is presented in Table S4 (SI). The first scan (Scan 0) and the last scan (Scan 29)  
319 correspond to T=0 minute, and T=1 hour, respectively. Using the Rietveld Refinements data  
320 allow obtaining a quantitative phase ratio for all scans (Figure 2 (b)). The evolution of the  
321 rhombohedral and the monoclinic phase percentage depending on the time exposure reveals a  
322 rapid rehydration up to 95% in less than 20 minutes. Moreover, the two phases co-exist at  
323 almost 50% after the exposure to humid argon for 7 minutes. As observed in previous studies,  
324 the intensity of the characteristic 011 peak of the monoclinic P2<sub>1</sub>/n phase is rising from the first  
325 scan until the last one, while the rhombohedral phase is diminishing with the rising amount of  
326 water molecules from the humid air.<sup>18,24,26,27</sup> Clavelin *et al.* showed a dehydrated rhombohedral  
327 structure evolving under laboratory ambient air exposure into monoclinic in about 30 min for  
328 compact powder and less than 5 min for an electrode.<sup>24</sup> Faster kinetics of rehydration is  
329 observed in the present study possibly due to the fact that the argon flow was forced through  
330 the capillary, while the hydration reaction was limited by diffusion of humidity from the  
331 ambient air in work.<sup>24</sup> Additionally, different rehydration mechanisms hypotheses in adsorption  
332 kinetics may be highlighted : first, the water insertion inside the most accessible interstitial  
333 sites, associated with the water adsorption at the surface and then the water transfer from the  
334 surface to the interstitial sites. After 20 minutes, the rehydration process presents lower kinetics.  
335 The water transfer may be impeding with time upon filling the reactive sites.



336 Tables S5 to S34 show all refinements parameters of the 30 refined scans from the SXRD  
 337 experiment. Scans 1 to 29 were refined with 2 phases (Space groups  $R\bar{3}$  and  $P2_1/n$ ), while scan  
 338 0 was only refined in the  $R\bar{3}$  space group, corresponding to the MnPW-D sample. These two  
 339 phases co-existed from the first minutes until the end of the experiment after one hour,  
 340 according to the observation of XRD profile shown in Figure S3 to Figure S5. Figure 2 (b)  
 341 shows that the percentage value of the rhombohedral  $R\bar{3}$  phase reaches 0% with Rietveld  
 342 refinement within one hour. However, the refinement of scan 29 shows that characteristic peak  
 343 012 of the dehydrated phase is still visible in a very low quantity, even after one hour exposed  
 344 to humid argon (Figure S5). The Rietveld refinement method would not quantify the residual  
 345 phase percentage. The residual rhombohedral phase observed after 1 hour under humidity  
 346 exposure is in line with the work by Li *et al.* <sup>27</sup>

347 The lattice volume evolution of the monoclinic and rhombohedral phase during the rehydration  
 348 process was followed (Figure 2 (c)). To ensure an accurate comparison, the lattice volume of  
 349 the monoclinic and the rhombohedral unit cells ( $V_C$  and  $V_R$ ) were converted into a cubic-based  
 350 one ( $V_C$ ). The volume is normalized in the cubic cell by using the following equations <sup>29</sup> :

$$351 \quad V_C = V_M \frac{(b_M^2 + c_M^2)}{b_M c_M \sin \beta}$$

$$352 \quad V_C = V_R \frac{4}{3}$$

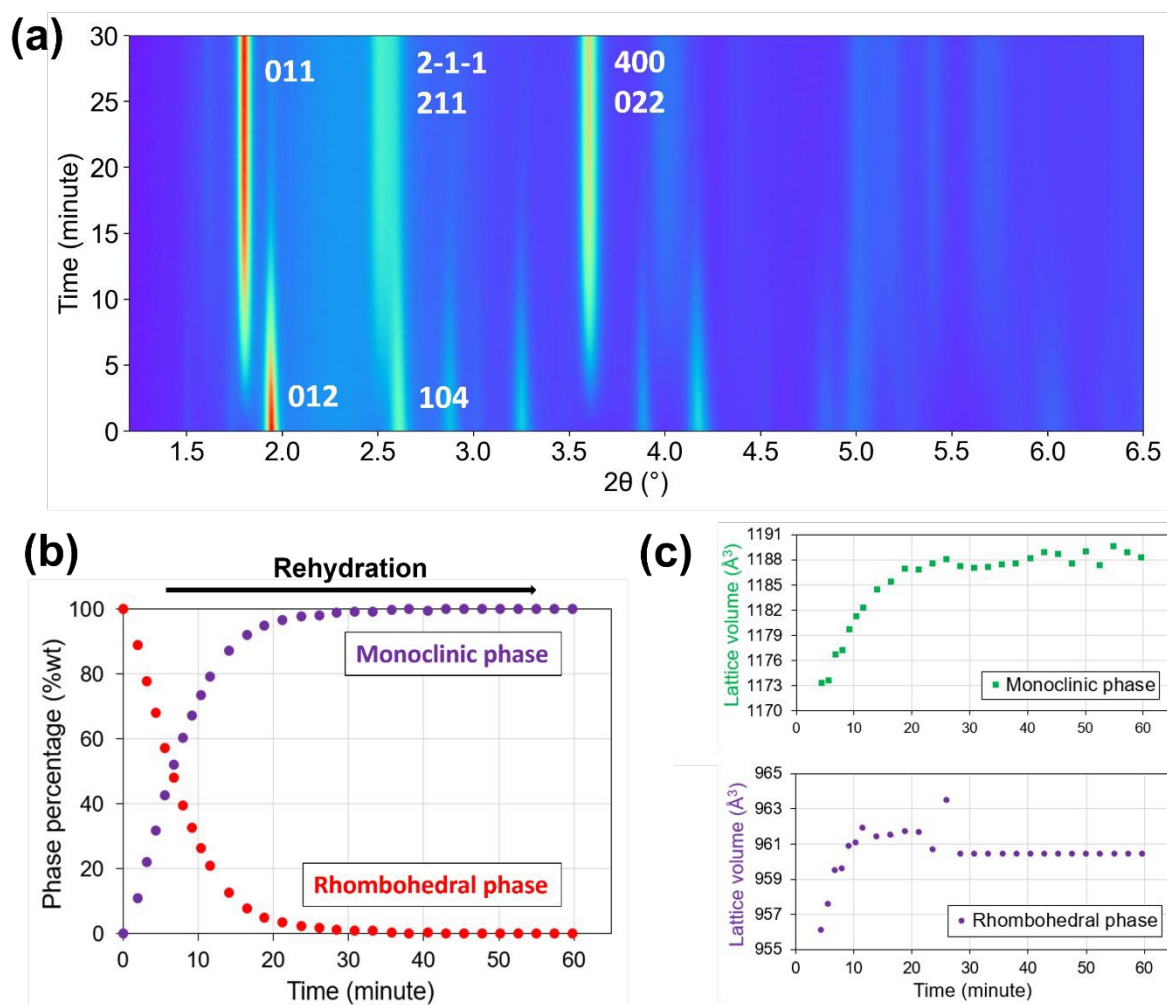
353 A slight increase of the lattice volume in the first 20 minutes reveals an expansion of the lattice  
 354 volume during the rehydration ( $\approx 15 \text{ \AA}^3$  for the monoclinic cell,  $\approx 5 \text{ \AA}^3$  for the rhombohedral  
 355 cell). Xiao *et al.* evidenced that the dehydration process induced stronger d- $\pi$  interactions  
 356 between Na and N by removing the water molecules, and hence reducing the volume of the  
 357 structure.<sup>30</sup> During the rehydration process, water molecules reinsert to the lattice, and may  
 358 cause the opposite effect with an increase of the lattice volume. The increase of water molecules  
 359 content is confirmed by the evolution of the water occupancy in the monoclinic phase during  
 360 the rehydration *in-situ* experiment (Figure S6). Furthermore, as seen on the same figure, the  
 361 rehydrated powder reveals a different monoclinic phase from the pristine one. The latter  
 362 exhibits thinner peaks with an average Full Width at Half Maximum (FWHM) of  $0.0259^\circ$  and  
 363  $0.0497^\circ$  for the rehydrated powder. Furthermore, Wang *et al.* demonstrated that the dehydration  
 364 process induced an increase of the  $[\text{Fe}(\text{CN})_6]$  vacancy defects, from 4% to 8% at  $190^\circ\text{C}$ .<sup>18</sup> The  
 365 increase of FWHM observed for the rehydrated sample could probably occur during the



366 dehydration process. Indeed, the dehydrated phase exhibits broad peaks (Figure S3(a))  
 367 suggesting the creation of a structural disorder during the dehydration step.

368 In order to study the complete rehydration of the sample, a dehydrated sample was exposed to  
 369 ambient air during 24 hours. The resulting sample is referred to as MnPW-R.

370

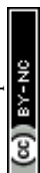


371

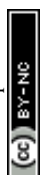
372 **Figure 2:** Structural parameters evolution during rehydration: *In-situ* XRD measurements as a function of  
 373 humidity-controlled atmosphere exposure on dried sample MnPW-D (a), evolution of the rhombohedral (red  
 374 dots) and the monoclinic phase (purple dots) depending on the time exposure at a dew point of  $-8^{\circ}\text{C}$  and with a  
 375 flow rate of  $30\text{ mL}\cdot\text{min}^{-1}$  (b), evolution of the lattice volume of the monoclinic cell (green marker) and the  
 376 rhombohedral cell (purple marker) during the rehydration (c). The lattice volume of the monoclinic and  
 377 rhombohedral cell is normalized in the cubic cell.

378

379 3.3. Influence of the interstitial water on PW's properties



380 Physical and electrochemical characterizations were performed on MnPW-H, MnPW-D and  
381 MnPW-R to clarify the impact of interstitial water on the material properties. First, *ex situ*  
382 SXR D analyses were additionally performed on MnPW-R (Figure S7). The crystal structure of  
383 MnPW-R is monoclinic in the  $P2_1/n$  space group. The MnPW-R pattern was refined by Rietveld  
384 method, confirming the space group  $P2_1/n$  with  $a = 10.584(2)$ ,  $b = 7.643(3)$ ,  $c = 7.304(3)$  Å,  
385 and  $\beta = 91.60(2)^\circ$ . Table S35 shows the refinement parameters of the MnPW-R sample from  
386 an *ex-situ* SXR D analysis. The observed pattern indicates that the rehydration is complete since  
387 the rhombohedral 012 peak at  $1.9^\circ$  totally disappears. MnPW-R *ex situ* SXR D pattern was  
388 compared to MnPW-H sample in Figure 3 (a) and the lattice parameters comparison between  
389 MnPW-H and MnPW-R is shown in Figure S8. A significant difference is observed for the  $b$ ,  
390  $c$  and  $\beta$  parameters, while the  $a$  parameter exhibit similar values. However, the lattice  
391 volumes of MnPW-H and MnPW-R samples are close ( $588(1)$  Å<sup>3</sup> and  $590(1)$  Å<sup>3</sup>, respectively).  
392 This phenomenon could be explained by the opposite balance of  $b$  and  $c$  parameters in the  
393 lattice, with the  $a$  position remaining stable. The two peaks between  $2.3^\circ$  and  $2.7^\circ$  and between  
394  $3.8^\circ$  and  $4.2^\circ$  are convoluted, which may be explained by the presence of broad peaks with an  
395 increase of the FWHM during the rehydration. This phenomenon can be attributed to the  
396 internal presence of residual strain or finer cracks. Beyond inducing internal structural changes  
397 at crystal lattice scale, the incorporation of water could have an impact on particle morphology.  
398 Therefore, SEM observations were performed on the three samples (Figure S9). Primary  
399 particles observations did not reveal major cracks on the dehydrated sample after the heat  
400 treatment of  $180^\circ\text{C}$  under vacuum, and reveal similar cubic shapes for the three samples. These  
401 observations would mean that heat treatment does not induce macroscopic alterations.  
402 Moreover, the hypothesis of a third phase could be also taken in consideration in MnPW-R.  
403 Notably, a cubic crystallographic structure was reported for the material containing a low  $\text{Na}_x$   
404 content ( $x < 1.5$ ), caused in some cases by a high concentration of  $\text{FeCN}_6$  vacancies.<sup>10,11,25,31</sup>  
405 Since we may have a lower amount of Na ions, a cubic phase could emerge between the  
406 convoluted double peaks with the loss of Na ions during the rehydration.<sup>11,25,31</sup> To evaluate this  
407 hypothesis, Mössbauer spectra were acquired on MnPW-H, MnPW-D and MnPW-R at 295 K  
408 (Figure S10). All three samples show the same single peak, corresponding to 100%  $\text{Fe}^{2+}$   
409 component. Since a loss of Na ions induce an oxidation of transition metal (Mn or Fe), the  
410 possible loss of Na ions in the rehydrated material MnPW-R could be due to Mn oxidation.  
411 Hence, it would be interesting to realize XAS or XPS analyses in order to evaluate the oxidation  
412 state of the Mn. To summarize, this rehydration phenomenon suggests an irreversible  
413 transformation considering the lattice parameters, and a disordered monoclinic phase which



414 presents a higher disorder than the as-synthesised one. Additionally, Table S1 and S35 reveal  
415 similar oxygen occupancy and atomic positions, suggesting a reversible insertion – deinsertion  
416 water molecules process after 24h under ambient air.

417 In order to highlight the differences in water content of the three samples, TGA was performed  
418 on MnPW-H, MnPW-D and MnPW-R (Figure 3 (b)). The MnPW-D TGA curve shows a lack  
419 of adsorbed and interstitial water in the structure. However, a residual water amount can be  
420 highlighted until 280°C ( $\approx 2\%$  of weight loss). MnPW-R exhibits three main weight losses,  
421 similarly to MnPW-H: the first between 0 and 150°C corresponding to the adsorbed water, the  
422 second from 150 °C to 220 °C attributed to the interstitial water release and the third from 280  
423 °C until 500°C associated with structure decomposition.<sup>10,24,32</sup> The higher amount of adsorbed  
424 water in MnPW-R compared to MnPW-H is confirmed by the gradual weight decrease of about  
425 6% up to 150 °C. Additionally, MnPW-R shows a slight lower amount of water filling the  
426 interstitial sites (8%) compared to MnPW-H (11%). Globally, MnPW-R exhibits a total weight  
427 loss of 14% corresponding to approximately 2.3 H<sub>2</sub>O molecules per formula unit, hence it  
428 incorporates less interstitial water than the hydrated phase, although rehydration is complete  
429 (Figure S7). Regarding the region above 280°C, MnPW-D and MnPW-R exhibit similar weight  
430 losses above 280°C (around 7% weight loss). Regarding MnPW-R, two weight losses are  
431 visible: the first contribution is weak and may be due to a low quantity of re-inserted  
432 coordinated water, while the second predominantly arises from structural decomposition.  
433 Hence, after dehydration and rehydration, the weight losses are identical and correspond mainly  
434 to the structure decomposition because the coordinated water was removed.<sup>33</sup>

435 The existence and amounts of adsorbed and interstitial water were further confirmed by ATR-  
436 FTIR. Figure 3 (c) shows the typical water spectral features in MnPW-H, D and R samples. The  
437 comparison of characteristic peaks, e.g. O-H stretching and H-O-H bending (3600 cm<sup>-1</sup> and  
438 1618 cm<sup>-1</sup>, respectively), reveals the removal of adsorbed and interstitial water in the structure  
439 with a lack of characteristic peaks in MnPW-D spectrum. Similarly to MnPW-H, water  
440 characteristic peaks at 1620 cm<sup>-1</sup>, 3527 cm<sup>-1</sup> and 3600 cm<sup>-1</sup> on the MnPW-R spectrum confirms  
441 the presence of adsorbed and interstitial water in the sample structure. Additionally, sharp peaks  
442 at 592 cm<sup>-1</sup> and 449 cm<sup>-1</sup> are indexed to be Fe-CN and Fe-C bonds, respectively, on the three  
443 samples profiles.<sup>10</sup> A residual peak attributed to ambient CO<sub>2</sub> is observed at 2350 cm<sup>-1</sup> in the  
444 MnPW-D infrared spectrum. Although a background spectrum was recorded prior to the  
445 measurement, fluctuations in atmospheric CO<sub>2</sub> concentration can still affect the result. Figure  
446 3 (d) shows bond vibrations evolution under air exposure through ATR-FTIR measurements.



447 MnPW-D features a  $C\equiv N$  triple bond characteristic peak at  $2046\text{ cm}^{-1}$  which shifted to higher  
448 wavenumber (lower energy of the bond) after the dehydration process. The removal of water  
449 molecules may induce a change in electronic environment of the  $C\equiv N$  bond with water  
450 molecules, indicated by a peak shift. It is also interesting to notice that the  $C\equiv N$  bond splits into  
451 at least two convoluted peaks during the rehydration of the sample at ambient air, similarly as  
452 the hydrated sample. Hence, a reversible phenomenon at bond scale is observed from MnPW-  
453 H to MnPW-R sample curves.

454 So far, the rehydration process induced irreversible internal structural effects but a reversible  
455 water capture process through TGA analysis. To further understand the (ir)reversibility of  
456 water-induced transformations, structural evaluations after several dehydration and rehydration  
457 cycles are necessary. Two samples MnPW-D2 and R2 were prepared, respectively, e.g. MnPW-  
458 R is dehydrated at  $180^\circ\text{C}$  under vacuum (D2), and then exposed again at ambient air for one  
459 day (R2). Another identical cycle yielded samples D3 and R3. The amount of water captured  
460 by these seven samples is first evaluated by TGA (Figure S11 (a)). MnPW-D, MnPW-D2, and  
461 MnPW-D3 TGA curves show a lack of adsorbed or interstitial water in the structure. A residual  
462 amount can be still observed around  $200^\circ\text{C}$  ( $\approx 2\%$  of weight loss). MnPW-R2 and MnPW-R3  
463 exhibit three distinct weigh losses, between 0 and  $150^\circ\text{C}$  (adsorbed water), from  $150^\circ\text{C}$  to  $200^\circ\text{C}$   
464 ( $^\circ\text{C}$  (interstitial water) and between  $300^\circ\text{C}$  to  $380^\circ\text{C}$  (removal of coordinated water and  
465 structure decomposition), similarly to MnPW-R.<sup>10,24</sup> Moreover, a slight higher total weight loss  
466 of 13% is highlighted for both compound, corresponding to 2.25  $\text{H}_2\text{O}$  molecules per formula  
467 unit, compared to MnPW-R. MnPW-R2 and MnPW-R3 curves exhibit a similar behaviour as  
468 MnPW-R, with a higher amount of adsorbed water and a lower amount of interstitial water,  
469 compared to MnPW-H.

470 Furthermore, the three rehydrated XRD analysis (Figure S11 (b)) exhibits similar XRD profiles  
471 for all rehydrated samples after one day, with peak width as broad as MnPW-R. The evolution  
472 of the normalized intensities is non-significant since the evolution is not linear. Hence, a  
473 structural transformation occurs during the first dehydration-rehydration cycle (MnPW-R),  
474 while the structure disorder remains stable over two additional cycles, as well as a similar  
475 amount of interstitial water captured (MnPW-R2 and R3).

476 The rehydration process triggers an irreversible transformation, yielding a disordered  
477 monoclinic phase distinct from the as-synthesized material, as reflected in its modified lattice  
478 parameters. Additionally, FT-IR analyses highlights a reversible phenomenon at bond scale



479 while MnPW-R shows a lower amount of water filling the interstitial sites compared to MnPW-  
 480 H.

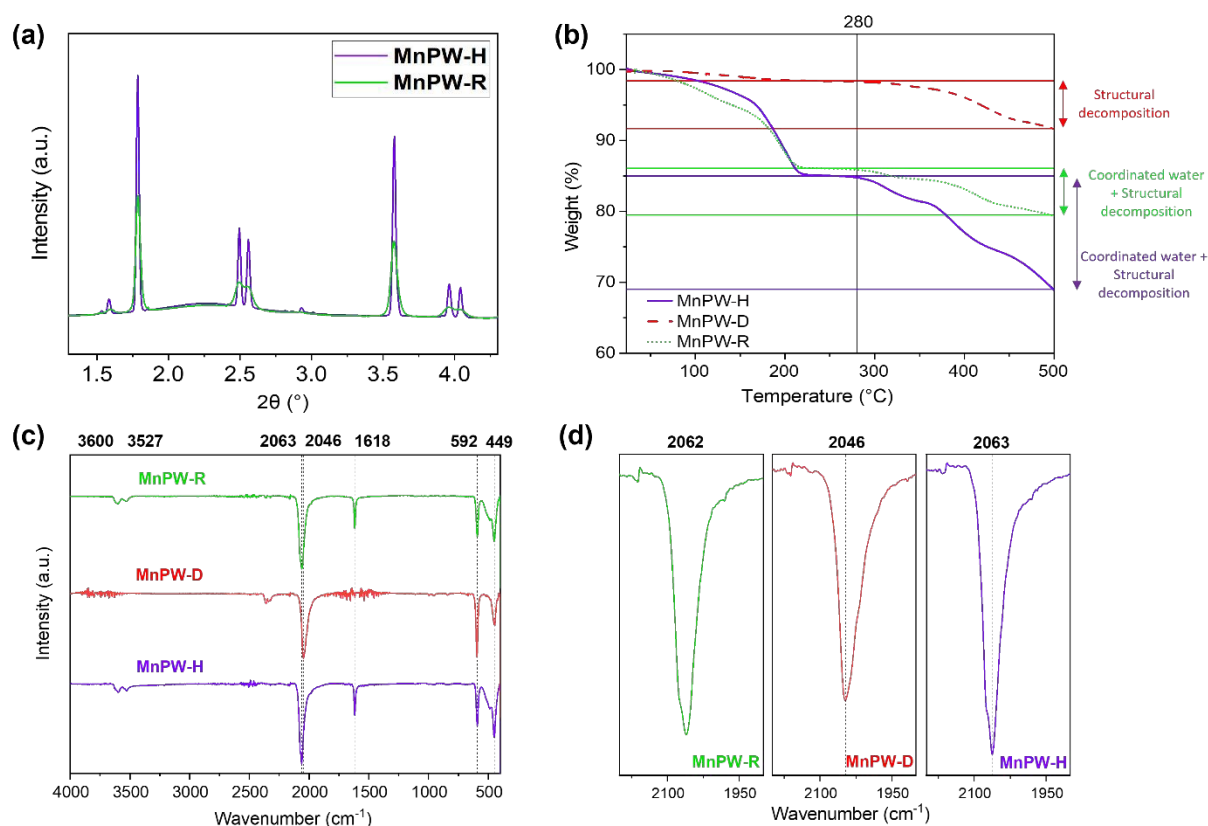


**Figure 3** : Comparative properties of samples with differing water content: XRD patterns of MnPW-H (purple) and MnPW-R (green) (a), TGA analysis at  $10\text{ }^{\circ}\text{C}\cdot\text{min}^{-1}$  under argon atmosphere until  $500\text{ }^{\circ}\text{C}$  (b), ATR-FTIR measurements (c) and zoom on C-N peak (d) of MnPW-H, MnPW-D and MnPW-R

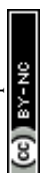
### 3.4. Influence of water on electrochemical performance

487 The electrochemistry was studied to understand the influence of water molecules on the cycling  
 488 performance. Figure 4 shows sodium insertion and extraction behaviour through galvanostatic  
 489 measurements of MnPW-H, MnPW-D and MnPW-R. The sodium half-cells were charged and  
 490 discharged with CC-CV mode with a top-off voltage at 4 V. First discharge capacity profile as  
 491 a function of the potential (vs  $\text{Na}^+/\text{Na}$ ) is shown on Figure 4 (a) in a voltage range of  $2.5\text{ V} \leq V$   
 492  $\leq 4\text{ V}$  at a C-rate of 0.1 C. MnPW-D exhibits a high first discharge capacity value of  $145\text{ mAh}\cdot\text{g}^{-1}$   
 493  $^1$  with an average potential of 3.5 V versus  $\text{Na}^+/\text{Na}$ . Knowing that the sodium content of the  
 494 material is 1.67, it is in good agreement with the theoretical capacity of  $144\text{ mAh}\cdot\text{g}^{-1}$ . One  
 495 plateau is observed for both charge and discharge of MnPW-D sample, even though a second  
 496 plateau can be observed at around 3.4 V in discharge, which may correspond to the



497 deconvolution of the two reductions reactions of the manganese and then the iron.<sup>2</sup> MnPW-H  
498 and MnPW-R exhibit moderate first discharge capacity of 112 mAh.g<sup>-1</sup> and 115 mAh.g<sup>-1</sup>,  
499 respectively. Two plateaus are observed for both charge and discharge of MnPW-H and MnPW-  
500 R sample, corresponding to the deconvolution of the Fe and Mn oxidation reactions.<sup>2</sup> However,  
501 MnPW-H first charge cycle curve exhibits a second plateau at higher potential, resulting in  
502 higher polarization. In 2015, Song et al.'s study on the water content effect in a Na<sub>2</sub>-  
503  $\delta$ MnFe(CN)<sub>6</sub> · zH<sub>2</sub>O compound highlighted the role of the C≡N<sup>-</sup> anion rotation on the energy  
504 difference in oxidation reactions. The dehydration process induces a rhombohedral structure,  
505 involving a shorter Mn···Fe distance in the structure lattice. Hence, the rotation of the linear  
506 C≡N<sup>-</sup> anions from the Mn···Fe axes becomes more constraint and induces a different response  
507 of the High Spin (HS) Mn<sup>2+</sup>/Mn<sup>3+</sup> and Low Spin (LS) Fe<sup>2+</sup>/Fe<sup>3+</sup> couples' energies.<sup>10</sup> This  
508 phenomenon would explain the potential difference of the redox reactions of Fe and Mn  
509 between a hydrated and dehydrated compound.

510 Figure 4 (b) shows capacity retention of MnPW-H, MnPW-D, and MnPW-R between 2.9 V  
511 and 4.0 V versus Na<sup>+</sup>/Na. Surprisingly, MnPW-D and MnPW-R demonstrate similar capacity  
512 retentions, 61% and 64%, respectively. On the other hand, MnPW-H shows a very poor capacity  
513 retention of 14% after 100 cycles. As seen in the Figure 3(b), the MnPW-R powder (2.3 H<sub>2</sub>O)  
514 exhibits a slight lower global water content than the MnPW-H powder (2.5 H<sub>2</sub>O). Since the  
515 electrodes were dried at 80°C during 48h under vacuum before assembling coin cells, a part of  
516 adsorbed water may be removed and lead to a higher retention capacity, enhanced by a lower  
517 amount of water filling the interstitial sites of MnPW-R (8%) compared to MnPW-H (11%).  
518 To determine the real water content before cycling, Karl Fischer measurements were provided  
519 on pristine electrodes dried at 80°C before entering the glovebox. An amount of 96550 ppm  
520 and 64698 ppm obtained for the MnPW-H and MnPW-R electrodes, respectively, confirms the  
521 lower interstitial water content in MnPW-R. One possible hypothesis might propose that the  
522 higher global water content in MnPW-H could explain the poorer capacity retention of this  
523 sample. However, the structure differences between these three samples must be taken into  
524 consideration. While MnPW-D has a capacity retention comparable to MnPW-R, both of the  
525 samples present a different structure, with a higher initial specific discharge capacity for  
526 MnPW-D. Moreover, as seen in the Figure 3(a), MnPW-R presents a disordered monoclinic  
527 phase with a higher disorder than the as-synthesised one. This rehydrated monoclinic phase  
528 with modified lattice parameters may lead to an alternative Na diffusion pathway in the  
529 structure, and might explain the higher capacity retention compared to MnPW-H over 100



530 cycles at low current density. As seen in the Figure S11, the structure disorder remains stable  
531 over two cycles of dehydration and rehydration, as well as a similar amount of interstitial water  
532 captured (MnPW-R2 and R3). Hence, beyond outperforming MnPW-H electrochemical  
533 stability, the MnPW-R phase may compete with the rhombohedral phase (MnPW-D) thanks to  
534 its structural stability.

535 Derivative curves of the discharge capacity are illustrated in Figure 4 (c). Different dQ/dV  
536 profiles are observed for hydrated and rehydrated compound. MnPW-H curve exhibits 3 peaks  
537 in charge at 3.37 V, 3.46 V and 3.70 V and 2 peaks in discharge at 3.2 V and 3.57 V. The redox  
538 reactions at 3.37 - 3.46/3.2V and 3.70/3.57V can be attributed to LS Fe<sup>2+</sup>/Fe<sup>3+</sup>, and HS  
539 Mn<sup>2+</sup>/Mn<sup>3+</sup> <sup>10,30,33,34</sup> The redox reactions of LS Fe<sup>2+</sup>/Fe<sup>3+</sup> at ≈3.4 V and HS Mn<sup>2+</sup>/Mn<sup>3+</sup> at ≈3.6  
540 V within the range of 2.5–4 V are slightly different to those of the rehydrated sample MnPW-  
541 R with 3.44/3.40 V and 3.67/3.57 V, respectively. After the reinsertion of water in the  
542 rehydrated sample, the redox reactions of low-spin Fe<sup>2+</sup>/Fe<sup>3+</sup> may partially activate, which can  
543 be seen at ≈3.4 V for MnPW-R and 3.3 V for MnPW-H.<sup>33</sup> This phenomenon could be linked  
544 with a general smaller amount of water for MnPW-R. MnPW-D curve exhibits one sharp  
545 oxidation peak at 3.55 V in the first charge process. However, as observed with the  
546 galvanostatic curve of MnPW-D, the reduction peak at 3.45 V becomes larger in discharge with  
547 the apparition of a second reduction peak observed at 3.4 V. This additional peak in discharge  
548 can be attributed to residual water in the structure, which is in agreement with TGA curve  
549 (Figure 3 (b)) exhibiting a small amount of water. The presence of water may also lead to a  
550 higher polarization for MnPW-H and MnPW-R, in comparison to MPW-D exhibiting a high  
551 polarization of 0.1 V.

552 In order to demonstrate the effect of the water molecules on Na<sup>+</sup> transport, the rate capability  
553 performance was evaluated at different current densities (Figure 4 (d)). The specific discharge  
554 capacity is plotted as a function of the cycle number to assess the electrochemical behaviour  
555 under various charge–discharge conditions (C/10, C/5, C, 5C). For the three samples, despite  
556 its good capacity retention at C/10, the capacity decreases abruptly at C and 5C. Additionally,  
557 MnPW-H exhibits lower capacity retentions on 5 cycles above C/10, in comparison to MnPW-  
558 R (89% vs 95% for C/10, 95% vs 98% for C/5, and 95% vs 98% for C). Compared to MnPW-  
559 D, the MnPW-R sample shows similar rate capability for the different C-rate, such as 95%,  
560 98%, 98% for C/10, C/5, and C, respectively. Overall, these results confirm that MnPW-R  
561 exhibits more stable electrochemical performance over a range of four current densities than  
562 MnPW-H. This statement reinforces the hypothesis of the effect of the lower amount of  
563 interstitial water in the MnPW-R sample, observed in the TGA analyses. Additional



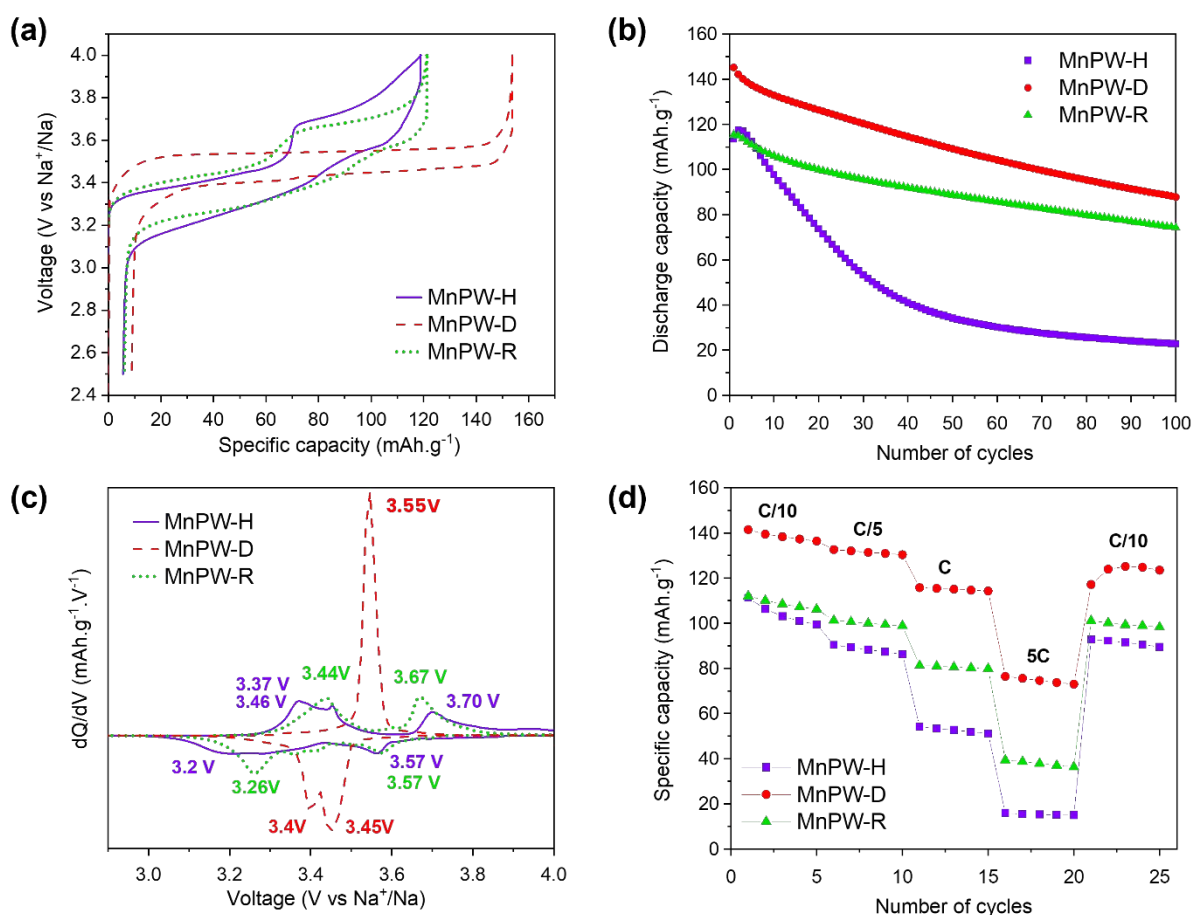
564 electrochemical characterizations were performed to strengthen the insight into the influence of  
565 water content on the structure. GITT and EIS analyses were presented in SI (Figure S12 and  
566 S13, respectively) to analyse the solid diffusion kinetics and the charge transfer resistance of  
567 MnPW-H, MnPW-D and MnPW-R. The curves of the GITT depending on the capacity and the  
568 time in the first charge and discharge cycle of MnPW-H, MnPW-D and MnPW-R are presented  
569 in the Figure S12 (a,b). Two plateaus at 3.4 V and 3.6 V are visible during the first charge for  
570 the hydrated and rehydrated sample, while MnPW-D exhibits one plateau at 3.55 V,  
571 corroborating the galvanostatic measurements. A zoomed-in view of the two plateaus are  
572 presented in the Figure S12 (c,d), and the corresponding  $D_{\text{Na}^+}$  values of the three samples were  
573 calculated. In the first plateau region, MnPW-H, MnPW-D, and MnPW-R exhibit a diffusion  
574 coefficient of  $6.7 \times 10^{-16} \text{ cm}^2 \cdot \text{s}^{-1}$ ,  $7.3 \times 10^{-16} \text{ cm}^2 \cdot \text{s}^{-1}$ , and  $2.6 \times 10^{-15} \text{ cm}^2 \cdot \text{s}^{-1}$ , respectively.  
575 Moreover, a diffusion coefficient of  $4.4 \times 10^{-17} \text{ cm}^2 \cdot \text{s}^{-1}$ ,  $2.0 \times 10^{-16} \text{ cm}^2 \cdot \text{s}^{-1}$ , and  $6.3 \times 10^{-17}$   
576  $\text{cm}^2 \cdot \text{s}^{-1}$  are determined for MnPW-H, MnPW-D and MnPW-R, respectively. Globally, the  
577 MnPW-H and MnPW-R diffusion coefficient values are higher on the first plateau region than  
578 the second one, indicating a higher  $\text{Na}^+$  diffusion kinetics when the charge begins. This second  
579 plateau would probably correspond to the water molecules removal and might explain the poor  
580 retention capacity in comparison to the literature.<sup>10,27</sup>

581 EIS spectra were collected for MnPW-H, MnPW-D, and MnPW-R before cycling, after 1 cycle,  
582 and after 5 cycles at C/10 (Figure S13). Before cycling, MnPW-H electrodes exhibit higher  
583  $\text{Re}(Z)$  than MnPW-D and MnPW-R even if the values suggest that it is dominated by the  
584 contribution of sodium metal (Figure S13 (a)). After the first and 5 cycles, the three samples  
585 show a significant increase in impedance, but MnPW-D and MnPW-R impedance values  
586 remain lower than MnPW-H, indicating increasing interfacial/SEI resistance and impeded  $\text{Na}^+$   
587 transport for MnPW-H (Figure S13 (b,c)). Overall, Figure S13 shows that the presence of water  
588 in MnPW-H increases the charge transfer resistance, thereby elevating the overpotential of the  
589 material.

590 Considering the electrochemical performance, the dehydrated compound is competitive in  
591 terms of first specific discharge capacity ( $145 \text{ mAh} \cdot \text{g}^{-1}$  at 0.1C). However, the material  
592 demonstrates capacity retention values below those reported in the literature. For example, Song  
593 *et al.* studied the electrochemical performance in a  $\text{Na}_{2.8}\text{MnFe}(\text{CN})_6 \cdot z\text{H}_2\text{O}$  compound at 0.7 C,  
594 reporting 75% capacity retention after 500 cycles.<sup>10</sup> Li *et al.* synthesized a  
595  $\text{Na}_{1.95}\text{Mn}[\text{Fe}(\text{CN})_6]_{0.91} \cdot 0.09 \cdot 0.08 \text{ H}_2\text{O}$  compound with a reversible capacity of  $157 \text{ mAh} \cdot \text{g}^{-1}$  at  
596 C/10 in a voltage range of 2.0 – 4.0 V vs  $\text{Na}/\text{Na}^+$ .<sup>27</sup> Clavelin *et al.* studied electrochemical  
597 performance of a dried PW  $\text{Na}_{1.87}\text{Mn}[\text{Fe}(\text{CN})_6]_{0.99} \cdot 1.99 \text{ H}_2\text{O}$  sample exhibiting a high specific



598 capacity of  $154 \text{ mAh.g}^{-1}$  (90% of the theoretical capacity) while the hydrated compound  
 599 presents an inferior specific capacity ( $125 \text{ mAh.g}^{-1}$ ). Furthermore, the capacity retention over  
 600 20 cycles at C/10 observed was 77%.<sup>24</sup> In this work, the sodium and  $\text{Fe}(\text{CN})_6$  content of the  
 601 initial compound ( $\text{Na} = 1.67$ ,  $\square = 0.88$ ) is lower than some reported in the literature. The poor  
 602 retention capacity of the three samples may be explained by the lack of 10% of  $\text{Fe}(\text{CN})_6$  or the  
 603 nature of the electrolyte causing unwanted side reactions. Wang *et al.*'s investigated the  
 604 electrochemical performance of rehydrated compounds. The compound synthesized in this  
 605 study is not comparable since iron partially occupies manganese sites. However, for a mostly  
 606 similar compound, Wang *et al.* showed poor retention capacity (41,5% over 500 cycles) for a  
 607 rehydrated compound after 10 minutes under ambient air exposure.<sup>18</sup> Hence, differences in  
 608 rehydration mechanisms can arise from differences in adsorption kinetics, e.g. results obtained  
 609 during the first hour differ from observations made after 24 hours as in our work.



610

611 **Figure 4** : Electrochemical performance of samples with different water content: Galvanostatic first charge and  
 612 discharge curves (a), capacity retention on 100 cycles (b),  $dQ/dV$  curves (c), and rate capabilities (d) of MnPW-  
 613 H (purple), MnPW-D (red) and MnPW-R (green) in a voltage range of  $2.5 \text{ V} \leq V \leq 4 \text{ V}$  vs  $\text{Na}^+/\text{Na}$  at a C-rate of  
 614  $0.1 \text{ C}$

615



## 616 4. Conclusions

View Article Online  
DOI: 10.1039/D5TA09250G

617 The structure of rehydrated Prussian White compound - a promising Na-ion battery electrode  
618 material - measured under ambient air exposure shows the presence of interstitial water in the  
619 lattice, which may alter ion insertion mechanisms during battery cycling process and cause  
620 performances losses. Here, we designed in situ high resolution synchrotron x-ray diffraction  
621 experiments coupled to humidity control to investigate the kinetics of water-induced structural  
622 changes in manganese-based PW  $\text{Na}_{2-x}\text{Mn}[\text{Fe}(\text{CN})_6]_y\text{H}_2\text{O}$  ( $0 \leq x \leq 2$ ) compound as a function  
623 of water quantity and establish the atomistic details of the sorption and desorption mechanisms.  
624 A controlled rehydration was applied to a dried compound in rhombohedral phase allowing  
625 observation of time-resolved structural evolution. Rietveld refinements analysis was used to  
626 extract volume changes and lattice parameters modifications, together with identification of  
627 novel phases.

628 An ultra-fast structure transformation takes place in twenty minutes in the conditions of the  
629 experiment, accompanied by the lattice volume expansion and appearance of a new monoclinic  
630 phase during the rehydration process. Hence, the rehydration process triggers an irreversible  
631 transformation, yielding a disordered monoclinic phase distinct from the as-synthesized  
632 material, as reflected in its broader peaks and modified lattice parameters. However, the lattice  
633 volume returns to its initial volume after completing the rehydration-dehydration process. A  
634 reversible insertion – deinsertion of water molecules is associated with the lattice volume  
635 evolution, highlighted by the similar oxygen occupancy and atomic positions of the hydrated  
636 and rehydrated samples after one day under air exposure. Additionally, a reversible rehydration  
637 process at bond scale is demonstrated through ATR-FTIR measurements. SEM observations  
638 shows the absence of macroscopic alterations. Therefore, the XRD pattern transformation can  
639 be attributed to internal structural (crystal scale), and to structural distortion during the  
640 dehydration and rehydration process, which could lead to an irreversible structural change. The  
641 lower amount of water filling the interstitial sites of MnPW-R, in comparison to the hydrated  
642 one, could be explained by the structural distortions and hindering the diffusion of water  
643 molecules into the interstitial sites located within the particle core. Regarding the  
644 electrochemical performance, promising first discharge capacities of  $145 \text{ mAh.g}^{-1}$  and  $112$   
645  $\text{mAh.g}^{-1}$  are obtained for the dried and hydrated PW, respectively, corresponding to 85% and  
646 66% of the theoretical capacity ( $171 \text{ mAh.g}^{-1}$ ). Surprisingly, MnPW-R and MnPW-D exhibit  
647 similar capacity retentions (64% and 61%), while MnPW-H retains only 14% of its initial  
648 capacity on 100 cycles at C/10 rate in a voltage range of 2.5 - 4 V vs  $\text{Na}^+/\text{Na}$ . The difference in



649 capacity retention values for MnPW-R and MnPW-H could be explained by the structural  
650 disorder occurring during the dehydration. The rehydrated monoclinic phase with modified  
651 lattice parameters may lead to a more stable phase (Figure S11). An alternative Na diffusion  
652 pathway in the structure might explain the higher capacity retention than MnPW-H over 100  
653 cycles. Hence, this study offers new insights into the impact of heat treatment on structural  
654 integrity of MnPW, and highlights new tracks of material optimisation to preserve the structure  
655 from destabilization at a long-term cycling.

656

657

### 658 **Author contributions**

659 The manuscript was written through contributions of all authors. All authors have given  
660 approval to the final version of the manuscript.

661 Léna PINEAU: Conceptualization; methodology; investigation; formal analysis; writing the  
662 original draft.

663 David PERALTA, and Loïc SIMONIN: Conceptualization, supervision, writing, reviewing,  
664 editing.

665 Irina PROFATILOVA: Methodology, resources, writing, review, editing.

666 Yohan BIECHER, Quentin JACQUET, Valentin VINCI: Methodology, formal analysis,  
667 review, editing.

668 Sandrine LYONNARD, Jakub DRNEC: Review, editing, project administration.

669

### 670 **Conflicts of interest**

671 There are no conflicts to declare.

672

### 673 **Data availability**

674 All data supporting the findings of this study, are provided in the supplementary information  
675 (SI) and can be shared upon request after publication.

676 The Synchrotron *in-situ* X-ray Diffraction dataset can be found at  
677 <https://doi.org/10.15151/ESRF-DC-2248221589>.

678

679

### 680 **Acknowledgements**



681 Beamtime at the ESRF was granted within the European Battery Hub MA6230. The authors  
682 acknowledge Florian Russello for his essential contribution in configuring the beamline setup.  
683 The authors also thank Gozde Oney for her valuable assistance with the XRD refinements. The  
684 authors are grateful to Martin Clemancey for his help with the Mössbauer analyses, and Dane  
685 Sotta for his contributions to the KF measurements.

686

687 **References**

- 688 1 J.-Q. Huang, R. Du, H. Zhang, Y. Liu, J. Chen, Y.-J. Liu, L. Li, J. Peng, Y. Qiao and S.-L.  
689 Chou, *Chem. Commun.*, 2023, **59**, 9320–9335.
- 690 2 C. D. Wessells, in *Les batteries Na-ion*, ISTE editions., 2021, pp. 297–347.
- 691 3 L. Wang, J. Song, R. Qiao, L. A. Wray, M. A. Hossain, Y.-D. Chuang, W. Yang, Y. Lu, D.  
692 Evans, J.-J. Lee, S. Vail, X. Zhao, M. Nishijima, S. Kakimoto and J. B. Goodenough, *J.*  
693 *Am. Chem. Soc.*, 2015, **137**, 2548–2554.
- 694 4 F. M. Maddar, D. Walker, T. W. Chamberlain, J. Compton, A. S. Menon, M. Copley and I.  
695 Hasa, *J. Mater. Chem. A*, 2023, **11**, 15778–15791.
- 696 5 X. Shen, X.-Q. Zhang, F. Ding, J.-Q. Huang, R. Xu, X. Chen, C. Yan, F.-Y. Su, C.-M.  
697 Chen, X. Liu and Q. Zhang, *Energy Mater Adv*, 2021, **2021**, 2021/1205324.
- 698 6 B. Wang, Y. Han, X. Wang, N. Bahlawane, H. Pan, M. Yan and Y. Jiang, *iScience*, 2018,  
699 **3**, 110–133.
- 700 7 X. Wu, W. Deng, J. Qian, Y. Cao, X. Ai and H. Yang, *J. Mater. Chem. A*, 2013, **1**, 10130.
- 701 8 B. Xie, B. Sun, T. Gao, Y. Ma, G. Yin and P. Zuo, *Coordination Chemistry Reviews*, 2022,  
702 **460**, 214478.
- 703 9 G. Goel, M. Sharma and S. K. Tripathi, *Journal of Energy Storage*, 2025, **126**, 116995.
- 704 10 J. Song, L. Wang, Y. Lu, J. Liu, B. Guo, P. Xiao, J.-J. Lee, X.-Q. Yang, G. Henkelman and  
705 J. B. Goodenough, *J. Am. Chem. Soc.*, 2015, **137**, 2658–2664.
- 706 11 J. Sottmann, F. L. M. Bernal, K. V. Yuseenko, M. Herrmann, H. Emerich, D. S. Wragg and  
707 S. Margadonna, *Electrochimica Acta*, 2016, **200**, 305–313.
- 708 12 C. D. Wessells, R. A. Huggins and Y. Cui, *Nat Commun*, 2011, **2**, 550.
- 709 13 D. Kim, A. Choi, C. Park, M.-H. Kim and H.-W. Lee, *J. Mater. Chem. A*, 2023, **11**, 13535–  
710 13542.
- 711 14 Y. Gao, Y. Huang, H. Pan, L. Ji, L. Wang, Y. Tang, Y. Zhu, M. Yan, G. Sun, W. Ni and Y.  
712 Jiang, *Journal of Alloys and Compounds*, 2023, **950**, 169886.
- 713 15 L. Hartmann, J. Deshmukh, L. Zhang, S. Buechele and M. Metzger, *J. Electrochem. Soc.*,  
714 2023, **170**, 030540.
- 715 16 Y. Yang, E. Liu, X. Yan, C. Ma, W. Wen, X.-Z. Liao and Z.-F. Ma, *J. Electrochem. Soc.*,  
716 2016, **163**, A2117–A2123.
- 717 17 M. G. Parma, H. Beraldo and I. de C. Mendes, *ACS Omega*, 2025, **10**, 11375–11385.
- 718 18 G. Wang, J. Zheng, K. Zhang, C. Zhang, J. Zheng, W. Fu, J. Wang, J. Li, M. Zhang, L.  
719 Meng, J. Wang and Z. Shen, *ACS Nano*, 2025, **19**, 22093–22108.
- 720 19 F. Peng, L. Yu, P. Gao, X.-Z. Liao, J. Wen, Y. He, G. Tan, Y. Ren and Z.-F. Ma, *J. Mater.*  
721 *Chem. A*, 2019, **7**, 22248–22256.
- 722 20 Y. Lu, L. Wang, J. Cheng and J. B. Goodenough, *Chem. Commun.*, 2012, **48**, 6544.
- 723 21 D. O. Ojwang, M. Svensson, C. Njel, R. Mogensen, A. S. Menon, T. Ericsson, L.  
724 Häggström, J. Maibach and W. R. Brant, *ACS Appl. Mater. Interfaces*, 2021, **13**, 10054–  
725 10063.



- 726 22 W. R. Brant, R. Mogensen, S. Colbin, D. O. Ojwang, S. Schmid, L. Häggström, T. Ericsson, A. Jaworski, A. J. Pell and R. Younesi, *Chem. Mater.*, 2019, **31**, 7203–7211. View Article Online  
DOI: 10.1039/D5TA09250G
- 727
- 728 23 I. Nielsen, D. Dzodan, D. O. Ojwang, P. F. Henry, A. Ulander, G. Ek, L. Häggström, T. Ericsson, H. L. B. Boström and W. R. Brant, *J. Phys. Energy*, 2022, **4**, 044012.
- 729
- 730 24 A. Clavelin, D. L. Thanh, I. Bobrikov, M. Fehse, N. E. Drewett, G. A. López, D. Saurel and M. Galceran, *ACS Materials Lett.*, 2024, **6**, 5208–5214.
- 731
- 732 25 I.-H. Jo, S.-M. Lee, H.-S. Kim and B.-S. Jin, *Journal of Alloys and Compounds*, 2017, **729**, 590–596.
- 733
- 734 26 K. Sada, S. M. Greene, S. Kmiec, D. J. Siegel and A. Manthiram, *Small*, 2024, **20**, 2406853.
- 735
- 736 27 Z. Li, Y. Wang, F. Rabuel, M. Deschamps, G. Rousse, O. Sel and J.-M. Tarascon, *Energy Storage Materials*, 2025, **76**, 104118.
- 737
- 738 28 S. N. Ghosh, *Journal of Inorganic and Nuclear Chemistry*, 1974, **36**, 2465–2466.
- 739
- 740 29 J.-H. Lee, J.-G. Bae, M. S. Kim, J. Y. Heo, H. J. Lee and J. H. Lee, *ACS Nano*, 2024, **18**, 1995–2005.
- 741
- 742 30 P. Xiao, J. Song, L. Wang, J. B. Goodenough and G. Henkelman, *Chem. Mater.*, 2015, **27**, 3763–3768.
- 743
- 744 31 H. Yao, Y. Gao, X. Lin, H. Zhang, L. Li and S. Chou, *Advanced Energy Materials*, 2024, 2401984.
- 745
- 746 32 W. Li, C. Han, W. Wang, Q. Xia, S. Chou, Q. Gu, B. Johannessen, H. Liu and S. Dou, *Advanced Energy Materials*, 2020, **10**, 1903006.
- 747
- 748 33 W. Wang, Y. Gang, J. Peng, Z. Hu, Z. Yan, W. Lai, Y. Zhu, D. Appadoo, M. Ye, Y. Cao, Q. Gu, H. Liu, S. Dou and S. Chou, *Adv Funct Materials*, 2022, **32**, 2111727.
- 749
- 750 34 L. Ge, Y. Song, P. Niu, B. Li, L. Zhou, W. Feng, C. Ma, X. Li, D. Kong, Z. Yan, Q. Xue, Y. Cui and W. Xing, *ACS Nano*, 2024, **18**, 3542–3552.
- 751



## Data availability

View Article Online  
DOI: 10.1039/D5TA09250G

All data supporting the findings of this study, are provided in the supplementary information (SI) and can be shared upon request after publication.

The Synchrotron *in-situ* X-ray Diffraction dataset can be found at <https://doi.org/10.15151/ESRF-DC-2248221589>.

